

Excitonic Chern insulator and kinetic ferromagnetism in MoTe₂/WSe₂ moiré bilayer

Zhihuan Dong¹ and Ya-Hui Zhang²

¹*Department of Physics, Massachusetts Institute of Technology, Massachusetts 02139, USA and*

²*Department of Physics and Astronomy, Johns Hopkins University, Baltimore, Maryland 21218, USA*
(Dated: February 9, 2023)

We propose a new mechanism for the quantum anomalous Hall (QAH) effect in the AB stacked MoTe₂/WSe₂ system. Based on the observation that the inter-layer tunneling is suppressed in the AB stacking, we consider a model with two layers coupled through the Coulomb interaction. The moiré lattices of the two layers are shifted to form a honeycomb lattice. Initially, the system is in a layer-polarized Mott insulator at $\nu_T = 1$. But with a displacement field, an equal number of holes and electrons are doped into the two layers respectively, forming inter-layer exciton condensation. Through mean field theory, we find $p \pm ip$ exciton condensation in a certain parameter regime, which leads to a Chern insulator with Chern number $C = \pm 1$. The valleys are polarized due to the kinetic energy instead of interaction. But the polarization in the two layers can be either the same or opposite. Especially, an inter-valley-coherent (IVC) Chern insulator phase is possible, in agreement with the recent magnetic circular dichroism (MCD) measurement. Our work opens a new direction to search for a topologically non-trivial excitonic insulator with high angular momentum exciton pairing symmetry.

Introduction Chern insulator is one of the famous topologically non-trivial states, which supports the quantum anomalous Hall (QAH) effect with a quantized Hall conductivity at zero magnetic field¹. Although the Chern insulator phase and QAH effect was theoretically proposed to be realized in the Haldane model in 1988², its experimental realization appeared only after 2013. The first realization is on the surface of the three-dimensional topological insulator³. The observations of the QAH effect⁴⁻¹⁰ in truly two-dimensional systems were achieved only a few years ago in the moiré systems^{4-6,9,11-27}.

QAH was first predicted theoretically for the graphene moiré systems²⁸. The moiré superlattice folds the original band into narrow moiré bands in a mini Brillouin Zone (MBZ). Especially the two valleys K and K' form their own moiré bands, which can have non-zero but opposite Chern numbers²⁸. Then the interaction can polarize the valley at filling $\nu_T = 1$ due to the Stoner ferromagnetism mechanism. After that, the Chern band of one valley is fully occupied, leading to a Chern insulator phase. After the experimental observations in several graphene systems⁴⁻¹⁰, many other theoretical studies²⁹⁻³⁹ confirm this simple picture as the mechanism for the QAH phase in graphene-based moiré systems. In this scenario, interaction is needed for valley ordering, but the band topology already exists at the single particle level. One natural question is then whether a Chern insulator phase is possible without single-particle band topology. We will propose a new mechanism towards QAH with band topology generated by exciton condensation, motivated by the recent experimental measurements of a QAH phase in a moiré system based on the AB stacked transition metal dichalcogenide (TMD) MoTe₂/WSe₂ bilayer^{27,40}.

In the AB stacked MoTe₂/WSe₂ hetero-bilayer^{27,40}, a Mott insulator evolves to a Chern insulator phase at den-

sity $\nu_T = 1$ per moiré unit cell when tuning the displacement field. There is evidence that the Chern insulator phase is in the regime where particles are transferred from the MoTe₂ layer to the WSe₂ layer, so the densities at the two layers are $1 - x$ and x respectively. Previous theories⁴¹⁻⁴⁷ all predict a phase with aligned valley polarizations in the two layers. Because these theories rely on a single particle tunneling term to couple the two layers to form a band, the valleys naturally align because the hopping term must be between the same valley due to momentum conservation. However, the recent experimental measurement of magnetic circular dichroism (MCD) indicates that the valleys in the two layers within the QAH phase are anti-aligned⁴⁰. It is clear that all of the previous theories are inconsistent with this measurement and a new theoretical explanation is needed for this system.

In this paper, we propose a completely new route towards QAH in AB-stacked TMD hetero-bilayer. Based on the observation that the inter-layer tunneling is suppressed in the AB stacking because the spin S_z in the two layers for the same valley are opposite (see Fig. 1(a)), we take the view that the most important coupling between the MoTe₂ and WSe₂ layer is the Coulomb interaction. The physics is then similar to the recently proposed^{48,49} and experimentally fabricated^{23,24} Coulomb coupled moiré bilayer. The major difference now is that the lattices of the two layers are shifted to form a honeycomb lattice together instead of being aligned. Then the electron and hole pockets in the two layers can form exciton condensation due to the inter-layer Coulomb interaction. In certain parameter regions, we find that the pairing symmetry of the exciton condensation is $p \pm ip$, similar to the $p \pm ip$ superconductor⁵⁰ after a particle-hole transformation only for one layer. This leads to a topological phase we dub excitonic Chern insu-

arXiv:2206.13567v3 [cond-mat.str-el] 7 Feb 2023

lator (ECI). In this case, we can have either intra-valley exciton condensation or inter-valley exciton condensation, which are nearly degenerate. With small valley contrasting flux of appropriate sign, inter-valley exciton condensation is selected and we reach an ECI phase with inter-valley-coherence (IVC), consistent with the MCD measurement⁴⁰. Our theory points out the possibility of a topological excitonic insulator phase with higher angular momentum exciton pairing symmetry, which was not well explored before.

Model For single-layer TMD, due to the Ising spin-orbit coupling, the spin and valley degrees of freedom are locked. For AB stacked MoTe₂/WSe₂ system, the spin-valley locking is opposite in the two layers, as shown in Fig. 1(a). For the WSe₂ or A layer, we have $(\tau_A^z, s_z) \in \{(K_A, \downarrow), (K'_A, \uparrow)\}$. For the MoTe₂ or B layer, we have $(\tau_B^z, s_z) \in \{(K_B, \uparrow), (K'_B, \downarrow)\}$. Here K_a, K'_a labels the two valleys for the layer $a = A, B$. τ_i, s_i with $i = x, y, z$ label Pauli matrices in the valley and spin space respectively. We also use σ_i with $i = x, y, z$ to label Pauli matrices in the layer space. In the following, the spin index will be ignored and the two valleys K, K' will be labeled as $+, -$. WSe₂ and MoTe₂ layers will be labeled as A, B .

We use a honeycomb lattice model for the MoTe₂/WSe₂ bilayer similar to Ref. 42, where Wannier orbitals from WSe₂ and MoTe₂ live on A and B sublattice sites (see Fig. 1(b)). The essential physics is captured by a simple lattice model:

$$\begin{aligned}
H = & -t_{AB} \sum_{\langle ij \rangle} (c_{i;\alpha}^\dagger c_{j;\alpha} + h.c.) + D \sum_i (-1)^{\sigma_z(i)} n_i \\
& - t_A \sum_{\langle\langle ij \rangle\rangle_A} (e^{i\phi_{ij}^A \tau_z} c_{i;\alpha}^\dagger c_{j;\alpha} + h.c.) \\
& - t_B \sum_{\langle\langle ij \rangle\rangle_B} (e^{i\phi_{ij}^B \tau_z} c_{i;\alpha}^\dagger c_{j;\alpha} + h.c.) \\
& + \frac{U}{2} \sum_i n_i (n_i - 1) + V \sum_{\langle ij \rangle} n_i n_j + V' \sum_{\langle\langle ij \rangle\rangle} n_i n_j \quad (1)
\end{aligned}$$

where $\alpha = +, -$ labels the valley index and we assume Einstein summation convention for α . $n_i = \sum_{\alpha=+,-} c_{i;\alpha}^\dagger c_{i;\alpha}$ is the density at site i . $\sigma_z(i) = 1, -1$ for A and B layer respectively. The two unit vectors of the lattice are $\mathbf{a}_1 = (1, 0)$ and $\mathbf{a}_2 = (-\frac{1}{2}, \frac{\sqrt{3}}{2})$. $\phi_{i; i+\mathbf{a}_1}^a = -\phi_{i; i-\mathbf{a}_1}^a = \phi_a$ is the valley contrasting hopping term for layer $a = A, B$. ϕ_{ij}^a of the other bonds are generated by C_3 symmetry. $\Phi_a = 3\phi_a$ is the valley contrasting flux through each triangle of the layer a . In the above $\langle ij \rangle$ labels the nearest neighbor AB bond. $\langle\langle ij \rangle\rangle_a$ labels the intra-layer nearest neighbor bond of the triangular lattice in the layer $a = A, B$. We expect $\phi_A \approx \frac{2\pi}{3}$ and $\phi_B \approx 0$ so that the band bottom of the two layers are at \mathbf{K}_M (\mathbf{K}'_M) and $\mathbf{\Gamma}_M$ in the mini Brillouin zone (MBZ). Time reversal symmetry flips the valley τ_z for both layers. Despite the superficial similarity to the model in Ref. 42 and Ref. 45, we will consider the limit $\frac{V}{t_{AB}} \rightarrow \infty$,

while the inter-layer interaction V term was ignored in Ref. 42 and Ref. 45.

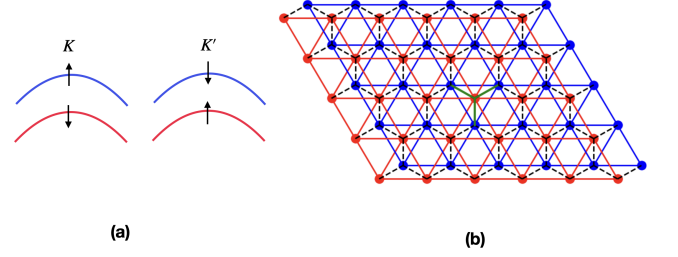


FIG. 1: (a) Illustration of the spin valley locking in MoTe₂/WSe₂ hetero-bilayer. Red and blue lines are the top valence band for the WSe₂ and MoTe₂ layer respectively. In AB stacking, one layer is rotated by 180° compared to AA stacking, which flips the spin-valley locking in this layer. (b) Lattice model on the honeycomb lattice. Red and blue labels A and B sublattice sites, corresponding to WSe₂ and MoTe₂ layer. The solid line is the nearest neighbor bond within each layer. The dashed line is the AB bond connecting the sites of the two layers. In our model, the microscopic hopping t_{AB} is assumed to be zero, but there can be effective inter-layer hopping spontaneously generated from exciton condensation. The exciton condensation order parameter is $\chi_{ij;\alpha\beta} = \langle c_{i;\alpha}^\dagger c_{j;\beta} \rangle$, where $\langle ij \rangle$ is illustrated as the green bond in (b).

In most of the paper, we assume $t_{AB} = 0$ for simplicity and will discuss its effect later. The global symmetry is then $U(1)^4$ at $t_{AB} = 0$, corresponding to the conservation of the four flavors combining layer and valley indices. If $\Phi_a = 0$, then the symmetry is enlarged to $U(1) \times U(2)$, with an $SU(2)$ rotation symmetry in the valley space only for the layer A . When $\Phi_A = \Phi_B = 0$, the symmetry is $U(2) \times U(2)$. When $t_{AB} = 0$, we are free to do a gauge transformation for only one layer to shift ϕ_a by $\pm \frac{2\pi}{3}$. Thus we can focus on the regime with $\phi_A \approx \phi_B \approx 0$. On the other hand, a finite t_{AB} reduces the symmetry to $U(1) \times U(1)$ with only total charge and total valley conservation for generic values of Φ_A, Φ_B . In this case, ϕ_A, ϕ_B can not be gauged away.

Let us focus on the filling with $\nu_T = n_A + n_B = 1$. Although in the experiment the valence band is hole-doped, here we use an electron picture after a particle-hole transformation. We start from large D where all of the electrons are in the B layer and there is a Mott insulator due to large U/t_B . When D is decreased, the B layer is hole-doped and the A layer has an equal number of electrons. A convenient way to deal with the large U term is to project to the Hilbert space without double occupancy and consider a bilayer t-J model:

$$\begin{aligned}
H = & -t_A \sum_{\langle\langle ij \rangle\rangle_A} (e^{i\phi_{ij}^A} \tau_z c_{i;\alpha}^\dagger c_{j;\alpha} + h.c.) + D \sum_{i \in A} n_i \\
& - t_B \sum_{\langle\langle ij \rangle\rangle_B} (e^{i\phi_{ij}^B} \tau_z P c_{i;\alpha}^\dagger c_{j;\alpha} P + h.c.) - D \sum_{i \in B} n_i \\
& + J_B \sum_{\langle\langle ij \rangle\rangle_B} \tau_i^\mu R_z^{\mu\nu} (2\phi_{ij}^B) \tau_j^\nu + (V' - \frac{J_B}{4}) \sum_{\langle\langle ij \rangle\rangle_B} n_i n_j \\
& + V \sum_{\langle ij \rangle} n_i n_j + V' \sum_{\langle\langle ij \rangle\rangle_A} n_i n_j \quad (2)
\end{aligned}$$

where P is the projection operator to forbid double occupancy. $R_z^{\mu\nu}(\phi)$ is the matrix representing rotation around z axis (see the supplementary⁵¹). For $U/t_B = 50^{45}$, $J_B = \frac{4t_B^2}{U} = 0.08t_B$. The effect of J_B is negligible. For simplicity, we do not impose a double-occupancy constraint for the A layer which is appropriate in the small n_A limit.

Phase diagram We can obtain a phase diagram by Hartree-Fock calculation directly for the Hubbard model in Eq. 1. We find valley polarization at an intermediate value of D and an excitonic Chern insulator (ECI) in a certain parameter regime. To make the mechanism of the magnetic order transparent, it is more convenient to work on the bilayer t-J model in Eq. 2 and use the Schwinger boson parton construction for the B layer: $c_{i;\alpha} = b_{i;\alpha} f_i$ with the constraint $\sum_\alpha b_{i;\alpha}^\dagger b_{i;\alpha} = f_i^\dagger f_i$ at each site $i \in B$. $b_{i;\alpha}$ is Schwinger boson carrying the valley degree of freedom while f_i is the spinless holon operator. The magnetic order at layer B is decided by the condensation of the Schwinger boson: $\begin{pmatrix} \langle b_{i;+} \rangle \\ \langle b_{i;-} \rangle \end{pmatrix} = F_i$. For valley ferromagnetic (FM) state with + valley, we use $F_i = \sqrt{n_a} \begin{pmatrix} 1 \\ 0 \end{pmatrix}$.

On the other hand, if there is a 120° anti-ferromagnetic (AF) order, we use $F_i = -\frac{\sqrt{n_a}}{\sqrt{2}} e^{\frac{i}{2}(\mathbf{Q} \cdot \mathbf{r}_i) \tau_z} \begin{pmatrix} 1 \\ 1 \end{pmatrix}$, where $\mathbf{Q} = \mathbf{K}_M$ or $-\mathbf{K}_M$. For the A layer, we assume full valley polarization as found in the Hartree Fock calculation. Then there is only spinless charge degree of freedom which we also label as f_i for $i \in A$.

After the magnetic orders are decided for both layers, the charge degree of freedom is conveniently captured by the following spinless model:

$$\begin{aligned}
H_f = & H_0^f + H_V^f \\
H_0^f = & - \sum_{a=A,B} \sum_{\langle\langle ij \rangle\rangle_a} t_{ij;a}^f f_i^\dagger f_j + D \sum_{i \in A} n_i - D \sum_{i \in B} n_i \\
H_V^f = & V \sum_{\langle ij \rangle} n_i n_j + \sum_{a=A,B} \sum_{\langle\langle ij \rangle\rangle_a} V' n_i n_j \quad (3)
\end{aligned}$$

where $t_{ij;B}^f = t_B (F_i^\dagger e^{i\phi_{ij;B} \tau_z} F_j)$ and $t_{ij;A}^f = t_A e^{i\phi_{ij;A} \tau_z}$. $n_i = f_i^\dagger f_i$ is constrained to be the physical density. The total filling is $n_A + n_B = 1$ so there are electron and

hole pockets in the two layers respectively. Due to the V term, we can decouple the following mean field:

$$H_M^f = -V \sum_{\langle ij \rangle} \chi_{ji} f_i^\dagger f_j \quad (4)$$

where $\chi_{ij} = \langle f_i^\dagger f_j \rangle$ is the exciton order parameter. The above term is basically a spontaneously generated hopping term on the nearest neighbor AB bond of the honeycomb lattice.

The obtained phase diagram is shown in Fig. 2(a), similar to the Hartree Fock results (see the supplementary). We find the following phases: (I) MI: layer polarized Mott insulator with 120° AFM in layer B; (II) FL: Fermi liquid with electron and hole pockets in A and B layer; (III) AF EI: excitonic insulator with AFM order in the B layer and τ_z FM order in the A layer. The Chern number is $C = 0$; (IV) NEI: nematic excitonic insulator with τ_z FM in both layers. The Chern number is $C = 0$; (V) ECI: excitonic Chern insulator with $|C| = 1$ and τ_z FM order in both layers. The transition between the trivial AF-EI and the topological ECI phase is first order with a small jump of the charge gap Δ_c .

Exciton order parameter and Chern number We allow various translational symmetry breaking patterns in the $\sqrt{3} \times \sqrt{3}$ unit cell and the exciton order parameter is in the form:

$$\chi_{ij} = \sum_{Q,L \in Z} \chi_{Q,L} e^{i\mathbf{Q} \cdot \mathbf{r}_i} e^{iL\theta(\mathbf{r}_j - \mathbf{r}_i)} \quad (5)$$

where $i \in A$ and $j \in B$. $\chi_{Q,L}$ is the amplitude. $\theta(\mathbf{r}_j - \mathbf{r}_i)$ is the angle of $\vec{r}_j - \vec{r}_i$ relative to the \hat{x} direction. Here Q and L are associated with the center of mass momentum and angular momentum of the exciton.

Both Q and L are not gauge-invariant. One can simply shift the momentum of each layer by a gauge transformation $f_{i;a} \rightarrow f_{i;a} e^{\pm i\mathbf{K}_M \cdot \mathbf{r}_i}$ with $a = A, B$ to shift Q and L . We define Q and L by going to the gauge which shifts the electron and hole pockets of the two layers to the Γ_M point of the MBZ⁵². In this gauge, the electron-hole problem can be mapped to the familiar Bardeen-Cooper-Schrieffer (BCS) theory of superconductor. Then we find there is only a $\mathbf{Q} = 0$ component, meaning that the exciton order can efficiently hybridize the electron and hole pockets at Γ_M point. The AF-EI has $L = 0$ or s wave exciton order. Its resulting band is trivial. The ECI phase is dominated by the $L = 1$ or $L = -1$ component and the exciton order is of $p \pm ip$ symmetry. This leads to a Chern band with $C = \pm 1$ and a QAH effect. In the NEI phase, the mixing between s ($L = 0$) and p ($L = \pm 1$) wave for the exciton order breaks the C_3 symmetry. The Chern number is zero. The exciton angular momentum is plotted in Fig. 2(b).

Let us also provide some intuitive explanations for why $p \pm ip$ exciton condensation is favored over the s wave. In the supplementary, we show that the competition between s wave and p wave exciton instability is decided by the magnitude of the form factors

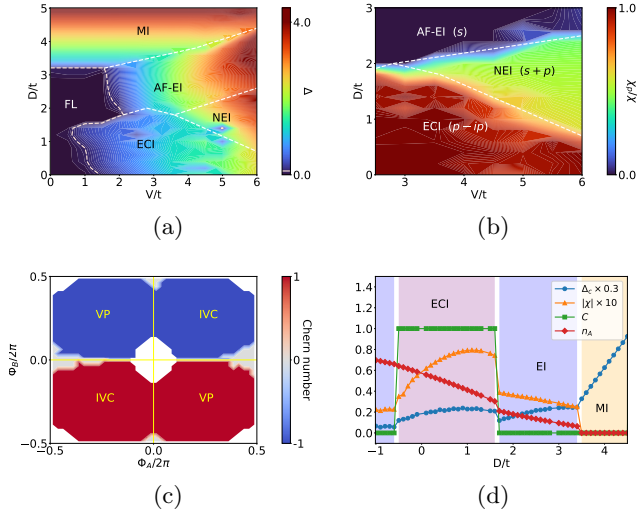


FIG. 2: (a) Schwinger boson mean field phase diagram in $D - V$ plane. The color bar shows the single electron charge gap Δ_c . Various phases are marked: Mott Insulator (MI), Fermi liquid (FL), trivial exciton insulator with nematicity (NEI), trivial exciton insulator with 120° order in B layer (AF-EI), excitonic Chern insulator with τ_z ferromagnetic order (ECI). In all of the three excitonic insulator phases, the A layer is valley polarized. (b) Evolution of exciton angular momentum. Colors show the weight of $p - ip$ (or $p + ip$) component. The ECI is dominated by $p \pm ip$ symmetry. NEI has a mixture of s and $p - ip$ waves so it breaks C_3 symmetry. (c) $\Phi_A - \Phi_B$ phase diagram for the Chern number. We used $D = 0.5, V = 4$. Metallic regions are whitened out. The model has time-reversal symmetry. We have restricted to the state with $\langle \tau_A^z \rangle > 0$. The corresponding valley-polarized (VP) and inter-valley-coherent (IVC) regions are marked with text. (d) Displacement field driven evolution along a line cut with $V = 2.5$. The transition from trivial to topological exciton insulating state is first order. Exciton order χ and charge gap Δ_c jumps on the phase boundary. The ECI phase onsets when n_A is above a critical density around 0.25. In the calculation, τ_A^z is fixed to be polarized to the $+$ valley. We use the following parameters: $U = 50, t_A = t_B = 1, \phi_A = \pi/4, \phi_B = \pi/12, V = 2V' = 4$. The results in (a) and (b) are calculated using Schwinger boson mean field theory, while (c) and (d) are obtained from Hartree-Fock mean field theory.

$F_l(\mathbf{k}) = \sum_{j=0,1,2} e^{i\frac{2\pi}{3}lj} e^{i\mathbf{k}\cdot\delta\mathbf{r}_j}$ near Fermi surfaces of the electron and hole pockets. Here $l = 0, 1, -1$ is the angular momentum of the exciton. $j = 0, 1, 2$ is summed over three nearest neighbor bonds and $\delta\mathbf{r}_j$ is the displacement vector of the nearest neighbor bond. When $n_A > 0.25$, we find that $|F_{l=\pm 1}(\mathbf{k})| > |F_{l=0}(\mathbf{k})|$ for \mathbf{k} around the Fermi surfaces of the electron and hole pockets. This agrees with our phase diagram in Fig. 2(a) where the

ECI phase onsets after a critical exciton density. We also find that a small valley flux Φ_A or Φ_B is needed to stabilize the ECI phase. For the $\Phi_A = \Phi_B = 0$ point, the ECI phase shrinks to a quite small regime in (D, V) parameter space (see the supplementary).

Kinetic magnetism and symmetry selection The ECI phase in the above is fully valley polarized in both layers. Unlike the quantum Hall ferromagnetism, there is no Hund's coupling or band topology in our model. Instead, the ferromagnetism is kinetically driven: with the valley polarization, the hopping of the holon f_i is larger, favored by the kinetic energy. This is similar to the celebrated Nagaoka ferromagnetism⁵³ in a hole-doped Mott insulator.

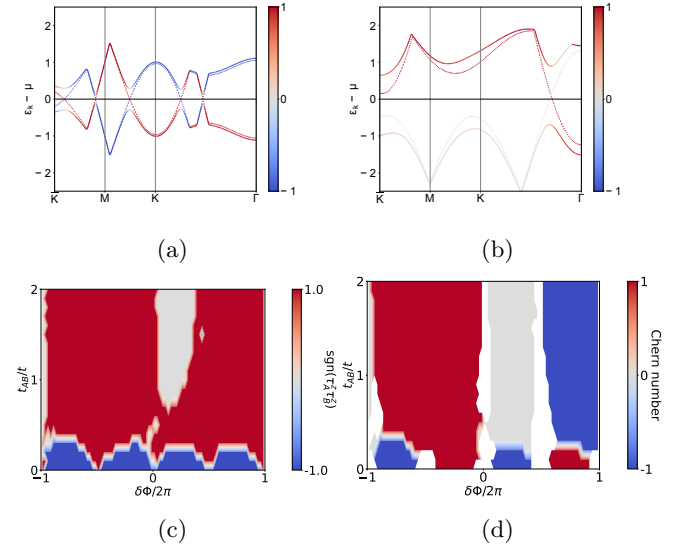


FIG. 3: Exciton gap opening and phase diagrams in $t_{AB} - \delta\Phi$ plane. (a),(b) Mean-field electron band structure in ECI and EI phases. Dotted and solid curves stand for band structures before and after turning on exciton order parameters. Colors show the valley polarization. (a) and (b) are obtained with $V = 1.5, D = 0.5$ and $V = 3, D = 3$ respectively. (c) The sign of $\tau_A^z \tau_B^z$ when it is nonzero. (d) Chern number. The gapless region is whitened out. In presence of t_{AB} , $\delta\Phi \rightarrow \delta\Phi + 2\pi$ is no longer a gauge transform. These phase diagrams are calculated using Hartree-Fock mean field for $t_A = t_B = 1, \Phi_A = 2\pi + \delta\Phi, \Phi_B = \delta\Phi, U = 50, V = 2V' = 4$ and $D = 0.5$.

The valley polarizations in two layers can have the same or opposite signs. At $\Phi_B = 0$ (or $\Phi_A = 0$), the valley SU(2) symmetry of the B (or A) layer guarantees the degeneracy of intra-valley and inter-valley exciton condensation. With a finite Φ_B , one of them is selected, while the other one is selected for an opposite sign of Φ_B because we can apply the transformation $i\tau_x$ only for layer B to flip Φ_B and τ_B^z together. This selection is shown in Fig. 2(c). For $\Phi_A \Phi_B > 0$, one finds that inter-valley exciton is favored and the QAH phase has

inter-valley-coherence(IVC) with $\tau_A^z \tau_B^z < 0$, consistent with the MCD measurement⁴⁰.

A finite t_{AB} can also lift the degeneracy and select the $\tau_A^z \tau_B^z > 0$ phase, as shown in Fig. 3(c). We need a finite but small valley flux Φ_A or Φ_B (as small as $\frac{\pi}{12}$) to stabilize the ECI phase. Deep inside the region with $\Phi_A \Phi_B > 0$, a sizable t_{AB} as large as 0.35 t is consistent with an ECI phase with opposite valley polarizations.

Lastly, our Schwinger boson formulation has the nice feature of spin-charge separation. In the supplementary, we show that increasing the superexchange J_B term can lead to an excitonic Chern insulator with canted spin texture and only partial valley polarization. This may be one explanation for the non-saturation of the MCD at a small magnetic field in the recent experiment⁴⁰. However, we note that partial valley polarization can also be trivially explained by domain wall formation driven by disorder effects.

Summary In conclusion we propose a new mechanism for the QAH effect in the Coulomb coupled moiré bilayer and apply it to the MoTe₂/WSe₂ system. In our model, the inter-layer hopping is spontaneously generated from inter-layer exciton condensation, which can have $p \pm ip$ symmetry and lead to an excitonic Chern

insulator (ECI). The ECI phase has valley ferromagnetism arising from kinetic energy, in contrast to the quantum Hall ferromagnetism picture for the QAH effect in graphene moiré systems^{28,31}. The valley polarizations in the two layers can be the same or opposite, depending on small perturbations away from a symmetric point where they are degenerate. Our theory opens a new direction to search for interaction-driven topological phases without single-particle band topology, for example in moiré bilayer with an hBN barrier in the middle. Excitonic insulators with $p \pm ip$ pairing symmetry may also be realized in other systems outside of the moiré materials.

Acknowledgement We thank Trithep Devakul, Liang Fu, and T. Senthil for useful discussions. We thank Kin Fai Mak and Jie Shan for their communications on their unpublished experimental data. ZD is supported by NSF grant DMR-1911666. YHZ is supported by a startup fund from Johns Hopkins University.

Note added When finalizing this manuscript, we become aware of a recent preprint⁵⁴ which also proposes inter-valley $p \pm ip$ exciton order for MoTe₂/WSe₂ system. But the mechanism to select the inter-valley exciton order over intra-valley exciton order in Ref. 54 relies on a large Hund's coupling and is different from our theory.

-
- ¹ C.-X. Liu, S.-C. Zhang, and X.-L. Qi, Annual Review of Condensed Matter Physics **7**, 301 (2016).
- ² F. D. M. Haldane, Phys. Rev. Lett. **61**, 2015 (1988).
- ³ C.-Z. Chang, J. Zhang, X. Feng, J. Shen, Z. Zhang, M. Guo, K. Li, Y. Ou, P. Wei, L.-L. Wang, et al., Science **340**, 167 (2013).
- ⁴ A. L. Sharpe, E. J. Fox, A. W. Barnard, J. Finney, K. Watanabe, T. Taniguchi, M. Kastner, and D. Goldhaber-Gordon, Science **365**, 605 (2019).
- ⁵ M. Serlin, C. Tschirhart, H. Polshyn, Y. Zhang, J. Zhu, K. Watanabe, T. Taniguchi, L. Balents, and A. Young, Science **367**, 900 (2020).
- ⁶ G. Chen, A. L. Sharpe, E. J. Fox, Y.-H. Zhang, S. Wang, L. Jiang, B. Lyu, H. Li, K. Watanabe, T. Taniguchi, et al., Nature **579**, 56 (2020).
- ⁷ S. Chen, M. He, Y.-H. Zhang, V. Hsieh, Z. Fei, K. Watanabe, T. Taniguchi, D. H. Cobden, X. Xu, C. R. Dean, et al., Nature Physics **17**, 374 (2021).
- ⁸ H. Polshyn, J. Zhu, M. A. Kumar, Y. Zhang, F. Yang, C. L. Tschirhart, M. Serlin, K. Watanabe, T. Taniguchi, A. H. MacDonald, et al., Nature **588**, 66 (2020).
- ⁹ H. Polshyn, J. Zhu, M. A. Kumar, Y. Zhang, F. Yang, C. L. Tschirhart, M. Serlin, K. Watanabe, T. Taniguchi, A. H. MacDonald, et al., Nature **588**, 66 (2020).
- ¹⁰ H. Polshyn, Y. Zhang, M. A. Kumar, T. Soejima, P. Ledwith, K. Watanabe, T. Taniguchi, A. Vishwanath, M. P. Zaletel, and A. F. Young, Nature Physics **18**, 42 (2022).
- ¹¹ Y. Cao, V. Fatemi, A. Demir, S. Fang, S. L. Tomarken, J. Y. Luo, J. D. Sanchez-Yamagishi, K. Watanabe, T. Taniguchi, E. Kaxiras, et al., Nature **556**, 80 (2018).
- ¹² G. Chen, A. L. Sharpe, P. Gallagher, I. T. Rosen, E. Fox, L. Jiang, B. Lyu, H. Li, K. Watanabe, T. Taniguchi, et al., arXiv e-prints, arXiv (2019).
- ¹³ G. Chen, L. Jiang, S. Wu, B. Lyu, H. Li, B. L. Chittari, K. Watanabe, T. Taniguchi, Z. Shi, J. Jung, et al., Nature Physics **15**, 237 (2019).
- ¹⁴ M. Yankowitz, S. Chen, H. Polshyn, Y. Zhang, K. Watanabe, T. Taniguchi, D. Graf, A. F. Young, and C. R. Dean, Science **363**, 1059 (2019).
- ¹⁵ X. Lu, P. Stepanov, W. Yang, M. Xie, M. A. Aamir, I. Das, C. Urgell, K. Watanabe, T. Taniguchi, G. Zhang, et al., Nature **574**, 653 (2019).
- ¹⁶ Y. Cao, D. Rodan-Legrain, O. Rubies-Bigorda, J. M. Park, K. Watanabe, T. Taniguchi, and P. Jarillo-Herrero, Nature **583**, 215 (2020).
- ¹⁷ X. Liu, Z. Hao, E. Khalaf, J. Y. Lee, Y. Ronen, H. Yoo, D. H. Najafabadi, K. Watanabe, T. Taniguchi, A. Vishwanath, et al., Nature **583**, 221 (2020).
- ¹⁸ C. Shen, Y. Chu, Q. Wu, N. Li, S. Wang, Y. Zhao, J. Tang, J. Liu, J. Tian, K. Watanabe, et al., Nature Physics, 1 (2020).
- ¹⁹ S. Chen, M. He, Y.-H. Zhang, V. Hsieh, Z. Fei, K. Watanabe, T. Taniguchi, D. H. Cobden, X. Xu, C. R. Dean, et al., Nature Physics **17**, 374 (2021).
- ²⁰ Y. Tang, L. Li, T. Li, Y. Xu, S. Liu, K. Barmak, K. Watanabe, T. Taniguchi, A. H. MacDonald, J. Shan, et al., Nature **579**, 353 (2020).
- ²¹ E. C. Regan, D. Wang, C. Jin, M. I. B. Utama, B. Gao, X. Wei, S. Zhao, W. Zhao, Z. Zhang, K. Yumigeta, et al., Nature **579**, 359 (2020).
- ²² L. Wang, E.-M. Shih, A. Ghiotto, L. Xian, D. A. Rhodes, C. Tan, M. Claassen, D. M. Kennes, Y. Bai, B. Kim, et al., Nature materials **19**, 861 (2020).
- ²³ J. Gu, L. Ma, S. Liu, K. Watanabe, T. Taniguchi, J. C.

- Hone, J. Shan, and K. F. Mak, *Nature Physics* **18**, 395 (2022).
- ²⁴ Z. Zhang, E. C. Regan, D. Wang, W. Zhao, S. Wang, M. Sayyad, K. Yumigeta, K. Watanabe, T. Taniguchi, S. Tongay, *et al.*, arXiv preprint arXiv:2108.07131 (2021).
- ²⁵ T. Li, S. Jiang, L. Li, Y. Zhang, K. Kang, J. Zhu, K. Watanabe, T. Taniguchi, D. Chowdhury, L. Fu, *et al.*, *Nature* **597**, 350 (2021).
- ²⁶ A. Ghiotto, E.-M. Shih, G. S. Pereira, D. A. Rhodes, B. Kim, J. Zang, A. J. Millis, K. Watanabe, T. Taniguchi, J. C. Hone, *et al.*, *Nature* **597**, 345 (2021).
- ²⁷ T. Li, S. Jiang, B. Shen, Y. Zhang, L. Li, Z. Tao, T. Devakul, K. Watanabe, T. Taniguchi, L. Fu, *et al.*, *Nature* **600**, 641 (2021).
- ²⁸ Y.-H. Zhang, D. Mao, Y. Cao, P. Jarillo-Herrero, and T. Senthil, *Phys. Rev. B* **99**, 075127 (2019).
- ²⁹ Y.-H. Zhang, D. Mao, and T. Senthil, *Phys. Rev. R* **1**, 033126 (2019).
- ³⁰ N. Bultinck, S. Chatterjee, and M. P. Zaletel, *Phys. Rev. Lett.* **124**, 166601 (2020).
- ³¹ C. Repellin, Z. Dong, Y.-H. Zhang, and T. Senthil, *Phys. Rev. Lett.* **124**, 187601 (2020).
- ³² H. C. Po, L. Zou, A. Vishwanath, and T. Senthil, *Phys. Rev. X* **8**, 031089 (2018).
- ³³ F. Wu and S. D. Sarma, *Phys. Rev. Lett.* **124**, 046403 (2020).
- ³⁴ F. Wu and S. D. Sarma, *Phys. Rev. B* **102**, 165118 (2020).
- ³⁵ J. Liu and X. Dai, *Phys. Rev. B* **103**, 035427 (2021).
- ³⁶ Y. Alavirad and J. Sau, *Phys. Rev. B* **102**, 235123 (2020).
- ³⁷ J. Shi, J. Zhu, and A. MacDonald, *Phys. Rev. B* **103**, 075122 (2021).
- ³⁸ J. Liu and X. Dai, *npj Computational Materials* **6**, 1 (2020).
- ³⁹ D. Mao and T. Senthil, *Phys. Rev. B* **103**, 115110 (2021).
- ⁴⁰ Z. Tao, B. Shen, S. Jiang, T. Li, L. Li, L. Ma, W. Zhao, J. Hu, K. Pistunova, K. Watanabe, *et al.*, arXiv preprint arXiv:2208.07452 (2022).
- ⁴¹ Y.-M. Xie, C.-P. Zhang, J.-X. Hu, K. F. Mak, and K. T. Law, *Phys. Rev. Lett.* **128**, 026402 (2022).
- ⁴² Y. Zhang, T. Devakul, and L. Fu, *Proceedings of the National Academy of Sciences* **118**, e2112673118 (2021).
- ⁴³ L. Rademaker, *Phys. Rev. B* **105**, 195428 (2022).
- ⁴⁴ H. Pan, M. Xie, F. Wu, and S. D. Sarma, arXiv preprint arXiv:2111.01152 (2021).
- ⁴⁵ T. Devakul and L. Fu, *Phys. Rev. X* **12**, 021031 (2022).
- ⁴⁶ Y.-W. Chang and Y.-C. Chang, arXiv preprint arXiv:2203.10088 (2022).
- ⁴⁷ Y. Su, H. Li, C. Zhang, K. Sun, and S.-Z. Lin, *Phys. Rev. R* **4**, L032024 (2022).
- ⁴⁸ Y.-H. Zhang, D. Sheng, and A. Vishwanath, *Phys. Rev. Lett.* **127**, 247701 (2021).
- ⁴⁹ Y.-H. Zhang, arXiv preprint arXiv:2204.10937 (2022).
- ⁵⁰ N. Read and D. Green, *Phys. Rev. B* **61**, 10267 (2000).
- ⁵¹ See Supplemental Material for details on Schwinger boson mean field theory.
- ⁵² This is a different gauge from the one we performed the Hartree Fock calculation, which shifts Φ_A, Φ_B to be close to zero.
- ⁵³ Y. Nagaoka, *Physical Review* **147**, 392 (1966).
- ⁵⁴ Y.-M. Xie, C.-P. Zhang, and K. T. Law, arXiv preprint arXiv:2206.11666 (2022).
- ⁵⁵ V. Kozii, M. P. Zaletel, and N. Bultinck, arXiv preprint arXiv:2005.12961 (2020).
- ⁵⁶ S. Chatterjee, T. Wang, E. Berg, and M. P. Zaletel, arXiv preprint arXiv:2109.00002 (2021).

Appendix A: Details on Hartree-Fock calculation of the Hubbard model

We start with the Hubbard model on the honeycomb lattice:

$$\begin{aligned}
H = & -t_{AB} \sum_{\langle ij \rangle} (c_{i,\alpha}^\dagger c_{j,\alpha} + h.c.) + D \sum_{i \in A} n_i - D \sum_{i \in B} n_i \\
& - t_A \sum_{\langle\langle ij \rangle\rangle_A} (e^{i\phi_{ij}^A \tau_z} c_{i,\alpha}^\dagger c_{j,\alpha} + h.c.) - t_B \sum_{\langle\langle ij \rangle\rangle_B} (e^{i\phi_{ij}^B \tau_z} c_{i,\alpha}^\dagger c_{j,\alpha} + h.c.) \\
& + \frac{U}{2} \sum_i n_i (n_i - 1) + V \sum_{\langle ij \rangle} n_i n_j + V' \sum_{\langle\langle ij \rangle\rangle} n_i n_j
\end{aligned} \tag{A1}$$

We can decouple the interaction part through mean-field ansatz:

$$\begin{aligned}
H_{HF} = & -t_{AB} \sum_{\langle ij \rangle} (c_{i,\alpha}^\dagger c_{j,\alpha} + h.c.) + D \sum_i (-1)^{\sigma_z(i)} n_i \\
& - t_A \sum_{\langle\langle ij \rangle\rangle_A} (e^{i\phi_{ij}^A \tau_z} c_{i,\alpha}^\dagger c_{j,\alpha} + h.c.) - t_B \sum_{\langle\langle ij \rangle\rangle_B} (e^{i\phi_{ij}^B \tau_z} c_{i,\alpha}^\dagger c_{j,\alpha} + h.c.) \\
& + U \sum_i (\rho_i c_{i,\alpha}^\dagger c_{i,\alpha} - \frac{1}{2} \rho_i^2) - U \sum_i (\tau_i^\mu c_{i,\alpha}^\dagger \tau_{\alpha\beta}^\mu c_{i,\beta} - \frac{1}{2} \tau_i^\mu \tau_i^\mu) \\
& + 2V \sum_{\langle ij \rangle} (\rho_j c_{i,\alpha}^\dagger c_{i,\alpha} - \chi_{ji,\beta\alpha} c_{i,\alpha}^\dagger c_{j,\beta} - \frac{1}{2} \rho_i \rho_j + \frac{1}{2} |\chi_{ij,\alpha\beta}|^2) \\
& + 2V' \sum_{\langle\langle ij \rangle\rangle} \rho_j c_{i,\alpha}^\dagger c_{i,\alpha} - \frac{1}{2} \rho_i \rho_j
\end{aligned} \tag{A2}$$

with self-consistent equations:

$$\begin{aligned}
\chi_{ij,\alpha\beta} &= \langle c_{i,\alpha}^\dagger c_{j,\beta} \rangle \text{ for } i, j \in \text{NN} \\
\rho_i &= \langle c_{i,\alpha}^\dagger c_{j,\alpha} \rangle \\
\tau_i^\mu &= \langle c_{i,\alpha}^\dagger \tau_{\alpha,\beta}^\mu c_{j,\beta} \rangle
\end{aligned} \tag{A3}$$

The mean field Hamiltonian is solved self-consistently. In addition, we use a $\sqrt{3} \times \sqrt{3}$ unit cell to allow states with translation symmetry breaking. In Fig.4, we show that the phase diagram from the Hartree-Fock calculation is consistent with the Schwinger boson mean field theory of the t-J model detailed in the following section. In the Hartree-Fock calculation, magnetic orders in both layers are self-consistently generated. We find that the A layer is fully valley-polarized from this self-consistent calculation.

Appendix B: Details on Schwinger boson calculation of the t-J model

In the limit of large U , the Hubbard model is approximated by a $t - J$ model

$$\begin{aligned}
H = & -t_A \sum_{\langle\langle ij \rangle\rangle_A} (e^{i\phi_{ij}^A \tau_z} c_{i,\alpha}^\dagger c_{j,\alpha} + h.c.) + D \sum_{i \in A} n_i \\
& - t_B \sum_{\langle\langle ij \rangle\rangle_B} (e^{i\phi_{ij}^B \tau_z} P c_{i,\alpha}^\dagger c_{j,\alpha} P + h.c.) - D \sum_{i \in B} n_i \\
& + J_B \sum_{\langle\langle ij \rangle\rangle_B} \tau_i^\mu R_z^{\mu\nu} (2\phi_{ij}^B) \tau_j^\nu + (V' - \frac{J_B}{4}) \sum_{\langle\langle ij \rangle\rangle_B} n_i n_j \\
& + V \sum_{\langle ij \rangle} n_i n_j + V' \sum_{\langle\langle ij \rangle\rangle_A} n_i n_j
\end{aligned} \tag{B1}$$

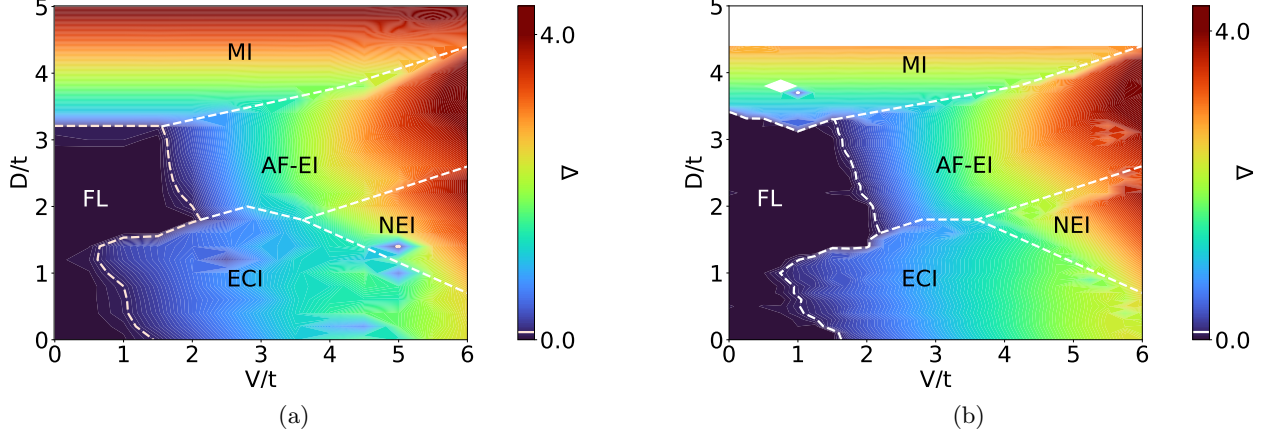


FIG. 4: Comparison between phase diagram from (a) t - J model treated with Schwinger boson mean field (b) Hubbard model treated with Hartree-Fock mean field. The color shows the charge gap. The two approaches are qualitatively consistent. MI is the layer-polarized Mott insulator with 120° anti-ferromagnetic order. FL is the Fermi liquid or electron-hole liquid. There are three different excitonic insulators: AF-EI, NEI, and ECI phase. τ_z is polarized in the A layer for all these three phases. The magnetic order in the B layer is 120° ordered in the AF-EI phase and τ_z polarized in the NEI and ECI phases. ECI has a $p \pm ip$ exciton condensation symmetry and a non-zero Chern number $C = \pm 1$, while NEI has $s + p$ pairing symmetry for the exciton condensation and zero Chern number.

where $J = \frac{4t^2}{U}$, and $R_z^{\mu\nu}$ is the matrix representing rotation around z axis, namely, $R(\phi) = \begin{pmatrix} \cos \phi & \sin \phi & 0 \\ -\sin \phi & \cos \phi & 0 \\ 0 & 0 & 1 \end{pmatrix}$ in the

basis of (τ_x, τ_y, τ_z) . Note that since A layer has a low density x , the double-occupancy projection P is not expected to be relevant. So we have treated the A layer as free fermions instead of using the composite degrees of freedom. In the calculation, we will set the magnetization in the A layer to be polarized along τ^z direction, which is found to hold throughout the Hartree-Fock phase diagram.

We use a fermionic holon, bosonic spinon construction for the B layer to take care of the projected operator: $c_{i\alpha} = b_{i\alpha} f_i$, with a constraint $n_i^f = n_i^b$. $b_{i\alpha}$ will be assumed to be condensed and just represents a magnetic order. This is just a convenient way to deal with the charge degree of freedom moving in the background of magnetic order. No exotic phase with fractionalization is targeted in our calculation. The Hamiltonian in Eq.2 is rewritten as

$$H = H_t + H_D + H_J + H_V \quad (\text{B2})$$

where

$$\begin{aligned} H_t &= -t_A \sum_{\langle\langle ij \rangle\rangle_A} (e^{i\phi_{ij}^A \tau_z} c_{i;\alpha}^\dagger c_{j;\alpha} + h.c.) + D \sum_{i \in A} n_i \\ &\quad - t_B \sum_{\langle\langle ij \rangle\rangle_B} (e^{i\phi_{ij}^B \tau_z} b_{i\alpha}^\dagger b_{j\alpha} f_i^\dagger f_j + h.c.) \\ H_D &= D \sum_{i \in A} f_i^\dagger f_i - D \sum_{i \in B} f_i^\dagger f_i \\ H_J &= J \sum_{\langle\langle ij \rangle\rangle} b_{i\alpha}^\dagger \sigma_{\alpha\beta}^\mu b_{i\beta} R_z^{\mu\nu}(\phi_{ij}) b_{j\gamma}^\dagger \sigma_{\gamma\delta}^\nu b_{j\delta} \\ H_V &= V \sum_{\langle ij \rangle} f_i^\dagger f_i f_j^\dagger f_j + V' \sum_{a=A,B} \sum_{\langle\langle ij \rangle\rangle_a} n_i n_j \end{aligned}$$

The exciton insulators found in Hartree-Fock always have τ_z polarization in the A layer. But the magnetic order of the B layer could be either 120° order or τ_z polarized FM order. To study the competition between the two magnetic orders of the B phase, we adopt the following ansatz for the Schwinger boson part

$$\begin{pmatrix} \langle\langle b_{i,+} \rangle\rangle \\ \langle\langle b_{i,-} \rangle\rangle \end{pmatrix} = F_i \quad (\text{B3})$$

with $F_i^A = \begin{pmatrix} 1 \\ 0 \end{pmatrix}$, $F_i^B = \sqrt{n_B} \begin{pmatrix} 1 \\ 0 \end{pmatrix}$ for the FM order. or $F_i^B = \sqrt{n_B} e^{\frac{i}{2}(\mathbf{Q} \cdot \mathbf{r}_i) \tau_z} \begin{pmatrix} \cos \frac{\theta}{2} \\ \sin \frac{\theta}{2} \end{pmatrix}$ for the canted AFM order, where $\mathbf{Q} = \mathbf{K}_M$ or $-\mathbf{K}_M$.

After the magnetic orders are decided for both layers, the charge degree of freedom is captured by a spinless model. We also label the valley polarized operator $c_{i,+}$ in the A layer as f_i with $i \in A$. The kinetic term is now

$$H_t^f = - \sum_{a=A,B} \sum_{\langle\langle ij \rangle\rangle_a} t_{ij;a}^f f_i^\dagger f_j + D \sum_{i \in A} f_i^\dagger f_i - D \sum_{i \in B} f_i^\dagger f_i \quad (\text{B4})$$

where $t_{ij;a}^f = t_a(F_i^{a\dagger} e^{i\phi_{ij;a} \tau_z} F_j^a)$. $n_i = f_i^\dagger f_i$ is constrained to be the physical density. The total filling is $n_A + n_B = 1$ so there are electron and hole pockets in the two layers respectively.

The H_J term simply contributes energy for each magnetic pattern:

$$H_J = J \sum_{\langle\langle ij \rangle\rangle_B} n_B \left(\cos^2 \theta + \sin^2 \theta \cos(2\phi_{ij} + \mathbf{Q} \cdot \mathbf{r}_{ij}) \right) \quad (\text{B5})$$

where $\mathbf{Q} = \Gamma_M, \mathbf{K}_M$ or $-\mathbf{K}_M$. Here θ is the angle between z -axis and the spin vector $\vec{\tau}_B$, and ϕ is the valley-contrasting hopping phase. H_V^{MF} term is taken care of by a mean-field decoupling

$$H_V = -V \sum_{\langle ij \rangle} \chi_{ij} f_i^\dagger f_j + h.c. - |\chi_{ij}|^2 \quad (\text{B6})$$

with self-consistent equation

$$\chi_{ij} = \langle f_i^\dagger f_j \rangle \quad (\text{B7})$$

The mean field energy is

$$\begin{aligned} H_{MF} = & - \sum_{a=A,B} \sum_{\langle\langle ij \rangle\rangle_a} t_a(F_i^{a\dagger} e^{i\phi_{ij;a} \tau_z} F_j^a) \chi_{ij} + h.c. + D \sum_{i \in A} \langle n_i \rangle - D \sum_{j \in B} \langle n_j \rangle \\ & - V \sum_{\langle ij \rangle} |\chi_{ij}|^2 + J \sum_{\langle\langle jj' \rangle\rangle_B} n_B \left(\cos^2 \theta + \sin^2 \theta \cos(2\phi_{jj'} + \mathbf{Q} \cdot \mathbf{r}_{jj'}) \right) \end{aligned} \quad (\text{B8})$$

The calculation proceeds in the following way. We target either FM or 120° AFM in the B layer and assume τ_z FM in the A layer, after that for each magnetic order pattern we deal with $H_t^f + H_V$ term with H_t^f in Eq. B4. We use a $\sqrt{3} \times \sqrt{3}$ unit cell, allowing the exciton order to break translation symmetry. In the end, for each magnetic order pattern, we add the spin coupling energy from the H_J term and compare their total energies. The phase diagram is shown in the main text.

Appendix C: Exciton order parameter

In this section, we discuss the symmetry of exciton order parameters. Following the Schwinger boson theory, we only need to consider a spinless model for the charge degree of freedom. The exciton arises from pairing between f_A and $h_B = f_B^\dagger$. This exciton order parameter

$$\chi_{ij} = \sum_{L,Q,\mathbf{k}} \langle f_{A,L\mathbf{K}+\mathbf{k}}^\dagger f_{B,L\mathbf{K}+Q\mathbf{K}+\mathbf{k}} \rangle e^{-i(L\mathbf{K}+\mathbf{k})(\mathbf{r}_i - \mathbf{r}_j) + iQ\mathbf{K}\mathbf{r}_j} \quad (\text{C1})$$

induces hybridization between A-layer particle pocket at $L\mathbf{K}$ and B-layer hole pocket at $(L+Q)\mathbf{K}$. We note in passing that Eq.5 in the main text is given by defining the Fourier transform

$$\chi_{Q,L} = \chi_{Q,L}(r_i, r_j) = \sum_{\mathbf{k}} \langle \chi_{\mathbf{k}}^{Q,L} \rangle e^{i\mathbf{k}(r_j - r_i)} = \sum_{\mathbf{k}} \langle f_{A,L\mathbf{K}+\mathbf{k}}^\dagger f_{B,L\mathbf{K}+Q\mathbf{K}+\mathbf{k}} \rangle e^{i\mathbf{k}(r_j - r_i)} \quad (\text{C2})$$

To extract the intrinsic exciton pairing angular momentum, we follow the convention of first shifting the band bottom of A and band top of B to the vicinity of Γ through a gauge transform,

$$\begin{aligned} f_{A,i} & \rightarrow f_{A,i} e^{-i\delta L\mathbf{K} \cdot \mathbf{r}_i} \\ f_{B,j} & \rightarrow f_{B,j} e^{-i(\delta L + \delta Q)\mathbf{K} \cdot \mathbf{r}_j} \end{aligned} \quad (\text{C3})$$

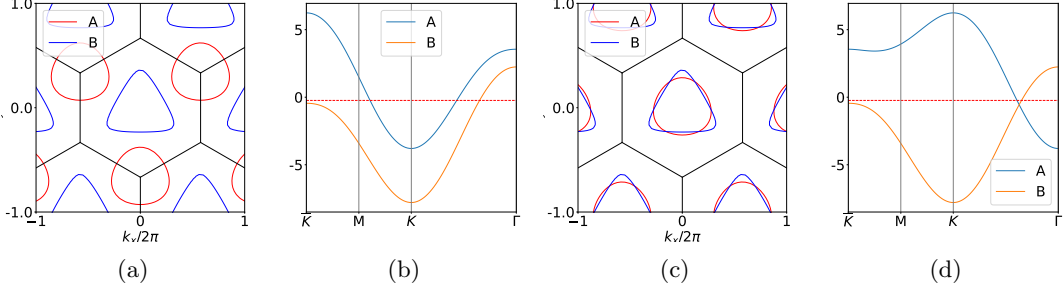


FIG. 5: Band structure and fermi surface without pairing for $D = 2.0$ (a)(b) $\phi_A = -\frac{7}{12}\pi$, $\phi_B = \frac{3}{4}\pi$, (c)(d) gauged to $\phi_A = \frac{1}{12}\pi$, $\phi_B = \frac{3}{4}\pi$. We choose the gauge under which the center of fermi pockets are at Γ . For this choice of ϕ_A, ϕ_B , the two fermi surfaces are perfectly nested after gauging, leading to a logarithmic divergence of exciton susceptibility. However, fermi liquid is still stable in this case for regions without full valley polarization.

For $\phi_A = (-2/3 + 1/12)\pi$, $\phi_B = (2/3 + 1/12)\pi$, the particle and holon pockets before and after gauge transform is shown in Fig.5 as an example.

We focus on the simple scenario with only one particle and one hole pocket. Then δL and $\delta L + \delta Q$ correspond to the band bottom of the A-layer and band top of the B-layer in the free model (before exciton condensation). After the gauge transform Eq.C3, exciton order should only couple two pockets at Γ_M , therefore it carries no momentum $Q' = Q - \delta Q = 0$. Now we are ready to read off the exciton order $\chi(\mathbf{k})$ from the Fourier transform of the gauged χ_{ij} .

To determine the large momentum δL and δQ for gauge transform, we note that the mean-field Hamiltonians for f_A and f_B are just two triangular lattice tight-binding models with only nearest-neighbor hopping,

$$\begin{aligned}
 H_A &= - \sum_{\langle i, i' \rangle_A} \tilde{t}^A e^{i\tilde{\phi}_{ii'}^A} f_i^{A\dagger} f_{i'}^A + h.c. \\
 H_B &= - \sum_{\langle j, j' \rangle_B} \tilde{t}^B e^{i\tilde{\phi}_{jj'}^B} f_j^{B\dagger} f_{j'}^B + h.c.
 \end{aligned} \tag{C4}$$

whose band top/bottom positions can be easily read off from the hopping phases $\tilde{\phi}_A, \tilde{\phi}_B$. (Here we use a tilde to distinguish from the valley contrasting phases in the original spinful model, these phases are the effective hopping phases for the charges once the spin gets integrated out.) Namely, the A-band bottom is at Γ_M for $\tilde{\phi}_A \in (-\pi/3, \pi/3)$, while the band top is at Γ_M for $\tilde{\phi}_B \in (2\pi/3, 4\pi/3)$. Furthermore, under the gauge transform Eq.C3 the $\tilde{\phi}$ transform as

$$\begin{aligned}
 \tilde{\phi}_{ii'}^A &\rightarrow \tilde{\phi}_{ii'}^A + \delta L \mathbf{K} \cdot (\mathbf{r}_i - \mathbf{r}_{i'}) \\
 \tilde{\phi}_{jj'}^B &\rightarrow \tilde{\phi}_{jj'}^B + (\delta L + \delta Q) \mathbf{K} \cdot (\mathbf{r}_j - \mathbf{r}_{j'})
 \end{aligned} \tag{C5}$$

and the order parameter becomes

$$\tilde{\chi}_{ij} = \chi_{ij} e^{i\delta L \mathbf{K} \cdot \mathbf{r}_i - i(\delta L \mathbf{K} + \delta Q \mathbf{K}) \cdot \mathbf{r}_j} \tag{C6}$$

Therefore our procedure for extracting pairing symmetries will be

- (1) For given a spin configuration F_i , extract the effective hopping phase $\tilde{\phi}_{A/B}^{ij} = \text{Arg}(\langle F_i | e^{i\phi_{A/B}^{ij} \sigma_z} | F_j \rangle)$
- (2) Find the $(\delta Q, \delta L)$ that sends $\tilde{\phi}_{A/B}$ to the proper ranges mentioned above.
- (3) Fourier transform the gauged exciton order $\tilde{\chi}_{Q'L'} = \tilde{\chi}_{ij} e^{iL' \mathbf{K} \cdot \mathbf{r}_i - i(L' \mathbf{K} + Q' \mathbf{K}) \cdot \mathbf{r}_j}$ to read off its remaining momentum Q' and angular momentum L' .
- (4) Fourier transform to extract $\tilde{\chi}(\mathbf{k}) = \sum_{ij} \tilde{\chi}_{ij} e^{i\mathbf{k}(\mathbf{r}_i - \mathbf{r}_j)} = \sum_{ij} \chi_{ij} e^{i(L\mathbf{K} + \mathbf{k})\mathbf{r}_i - i(L\mathbf{K} + Q\mathbf{K} + \mathbf{k})\mathbf{r}_j}$

Note that by gauging the pockets to Γ_M following step (2), we have basically picked a gauge under which the center of mass of the exciton pair carries momentum $\mathbf{Q} = 0$. In some cases, there can be coexisting p -wave and s -wave exciton orders. We extract each component through a Fourier transform for $\chi(\mathbf{k})$

$$\chi_l(|\mathbf{k}|) = \int d\theta_{\mathbf{k}} \chi(\mathbf{k}) e^{-il\theta_{\mathbf{k}}} \tag{C7}$$

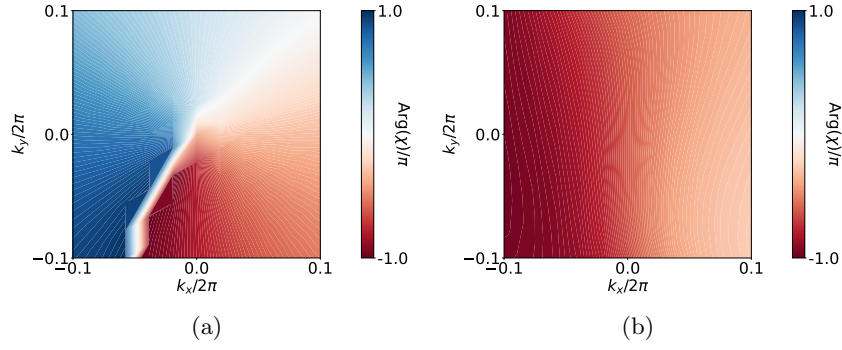


FIG. 6: Momentum space distribution of exciton. (a) $p + ip$ order of ECI at $D = 0.0$, $V = 6.0$ (b) $s + p$ -wave exciton order of EI at $D = 6.0$, $V = 2.0$. A strong nematicity is observed in the latter example. The transition from ECI to EI happens when the vortex in $\chi(\mathbf{k})$ gets pushed out of the small Fermi surface region by s -wave component. Plotted here is the phase of the gauged exciton order.

Alternatively, one can read off the strength of p/s wave orders from the (Q', L') Fourier components of χ_{ij} . In Fig.6 we show typical patterns of phase variation of exciton order χ in momentum space for the $p + ip$ ECI and $s + p$ nematic EI.

Appendix D: Competition between the s wave and p wave exciton condensation

In this section, we discuss why the p wave is favored over the s wave exciton condensation. The nearest neighbor interaction is decoupled into

$$H_V = -V \sum_{\langle ij \rangle} \chi_{ij}^* c_{i\sigma}^\dagger f_{j\sigma} + h.c. = -V \sum_{\mathbf{k}, l} \chi_l^* F_{\mathbf{k}}^l c_{i\alpha}^\dagger \sigma_{\alpha\beta}^\nu f_{j\beta} + h.c. \quad (D1)$$

where $F_{\mathbf{k}}^l = \sum_{\delta}^{NN} e^{il\theta_{\delta}} e^{-i\mathbf{k}\delta}$, and $\chi_l = \frac{1}{3} \sum_{\delta}^{NN} \chi_{\delta} e^{-il\theta_{\delta}}$. The self-consistent equation

$$\chi_l = \frac{1}{3} \sum_{\mathbf{k}, \omega} F_{\mathbf{k}}^{l*} \langle c_{\mathbf{k}}^\dagger f_{\mathbf{k}} \rangle \quad (D2)$$

$$= -\frac{1}{3} \sum_{\mathbf{k}, \omega} G^c(\mathbf{k}, i\omega) V \chi_m F_{\mathbf{k}}^m \tilde{G}^f(\mathbf{k}, i\omega) F_{\mathbf{k}}^{l*} \quad (D3)$$

$$= -\frac{V}{3} \sum_{\mathbf{k}, \omega} G^c(\mathbf{k}, i\omega) \tilde{G}^f(\mathbf{k}, i\omega) F_{\mathbf{k}}^{l*} F_{\mathbf{k}}^m \chi_m \quad (D4)$$

Here $G_c = (i\omega - \epsilon_{\mathbf{k}}^A)^{-1}$ and $\tilde{G}_f = (i\omega - \epsilon_{\mathbf{k}}^B - \Sigma_f(\mathbf{k}, i\omega))^{-1}$. This is an eigenvalue problem. The off-diagonal ($l \neq m$) contributions would be responsible for the $s + p$ wave exciton order observed. For notational simplicity, we will restrict ourselves to the diagonal part. Existence of a non-trivial solution for χ_l demands

$$\frac{1}{V} = - \sum_{\mathbf{k}, \omega} G^c(\mathbf{k}, i\omega) \tilde{G}^f(\mathbf{k}, i\omega) |F_{\mathbf{k}}^l|^2 / 3 \quad (D5)$$

$$= - \sum_{\mathbf{k}} \frac{f(\xi_{\mathbf{k},+}) - f(\xi_{\mathbf{k},-})}{\xi_{\mathbf{k},+} - \xi_{\mathbf{k},-}} |F_{\mathbf{k}}^l|^2 / 3 \quad (D6)$$

$$= - \int_{E_-}^{E_+} d^2\mathbf{k} \frac{|F_{\mathbf{k}}^l|^2 / 3}{\xi_{\mathbf{k},+} - \xi_{\mathbf{k},-}} \quad (D7)$$

$$= - \int_{E_-}^{E_+} d^2\mathbf{k} \frac{|F_{\mathbf{k}}^l|^2}{\sqrt{\delta_{\mathbf{k}}^2 + V^2 |\chi_l|^2 |F_{\mathbf{k}}^l|^2} / 3} \quad (D8)$$

In the third line, we have considered a simplest case with particle-hole symmetry $\epsilon_{\mathbf{k}}^{A/B} = \epsilon_F \pm \delta_{\mathbf{k}}/2$, namely the particle and hole pockets are perfectly nested. A short discussion of cases without perfect nesting will be presented later. Defining $\Phi_l(\mathbf{k}) = \frac{1}{\sqrt{3}}V\chi_l F_{\mathbf{k}}^l$, we find

$$\frac{1}{V} = - \int_{E_-}^{E_+} d^2\mathbf{k} \frac{|F_{\mathbf{k}}^l|^2}{\sqrt{\delta_{\mathbf{k}}^2 + 4\Phi_l^2(\mathbf{k})}} \quad (\text{D9})$$

This is analogous to the self-consistency equation for BCS instability. At zero temperature the logarithmic divergence of integral at $\Phi = 0$ indicates that an infinitesimal V would lead to exciton condensation. So the Fermi liquid is always unstable in the $V > 0$ regime. From Eq.D9 we obtain the scaling of exciton order

$$\chi^l \sim \frac{\rho(\epsilon_F)}{V\eta^l(\epsilon_F)} e^{-\frac{1}{2V\eta^l(\epsilon_F)}} \quad (\text{D10})$$

where $\eta(\epsilon_F)$ is the weighted average of form factor in channel l around the fermi surfaces

$$\eta^l(\epsilon_F) = \int_{FS} \frac{d\mathbf{k}_F}{(2\pi)^2} \frac{|F_{\mathbf{k}_F}^l|^2}{v_{\mathbf{k}_F}} \quad (\text{D11})$$

here the weight is the density of states. This expression reduces to

$$\eta^l(\epsilon_F) \sim \rho(\epsilon_F) \int_{FS} d\mathbf{k}_F |F_{\mathbf{k}_F}^l|^2 \quad (\text{D12})$$

in the small k_F limit where the band structure has an approximate rotational symmetry. The angular momentum channel of the condensed exciton is efficiently predicted by comparing the parameter $\eta^l(\epsilon_F)$ across all angular momentum channels $l = 0, 1, -1$.

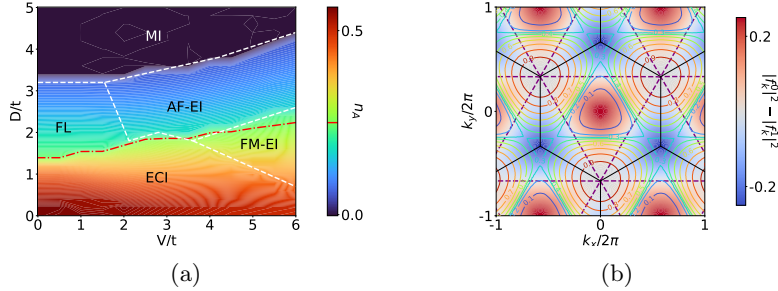


FIG. 7: (a) Exciton density. The contour in red corresponds to $n_{A(c)} = 0.25$. It closely tracks the onset of $p + ip$ order. (b) Difference between form factors in $l = 0$ and $l = 1$ channels. The purple dashed contour marks momentum where two form factors are equal. Overlaid contours show the Fermi surface at a sequence of exciton densities n_A . Above $n_A = 0.2$, the Fermi surface starts to pass through the area with a stronger p -wave form factor. At $n_A = 0.3$ the Fermi surface is predominantly through the blue area. Somewhere in between these two densities, the pairing instability should change from s -wave to p -wave. This estimation is consistent with the critical density read off from (a)

In the following, we explore the cases without nesting between particle and hole pockets. For convenience we denote the susceptibility $\Pi_{\mathbf{k}'} = \int d\omega G^A(\mathbf{k}', \omega) G^B(\mathbf{k}', \omega)$. Generally speaking, at the transition point $\chi = 0$, exciton susceptibility

$$\Pi_{\mathbf{k}} \sim - \frac{f(\epsilon_{\mathbf{k}}^A) - f(\epsilon_{\mathbf{k}}^B)}{\epsilon_{\mathbf{k}}^A - \epsilon_{\mathbf{k}}^B} \quad (\text{D13})$$

where $f(\epsilon) = (1 + e^{\beta(\epsilon - \epsilon_F)})^{-1}$ is the Fermi-Dirac distribution. The dominating contribution comes from the \mathbf{k} points with $\epsilon_{\mathbf{k}}^A = \epsilon_{\mathbf{k}}^B = 0$. For generic parameters (ϕ_A, ϕ_B) , the two fermi surfaces do not overlap, but the total filling $\nu_T = 1$ dictates that they intersect at $3N$ momentum points, where N is an even number. Assume $f_{\mathbf{k}}^l$ vary slowly in the vicinity of this spot. The dispersion is

$$\epsilon^A(k) = u_A k_x + v_A k_y, \quad \epsilon^B(k) = u_B k_x + v_B k_y \quad (\text{D14})$$

for simplicity we will take $u_A = -u_B = u$ and $v_A = v_B = v$, assume $u/v = \cot \theta > 1$, where 2θ is the angle between two fermi surfaces

$$\int_0^\Lambda d^2\mathbf{k} \Pi_{\mathbf{k}} = 4 \int_0^\Lambda dk_y \int_{\frac{v}{u}k_y}^\Lambda dk_x \frac{1}{2uk_x} = 2 \int_0^\Lambda dk_y \ln \frac{u\Lambda}{vk_y} = 2\Lambda(1 + \ln \frac{u}{v}) \quad (\text{D15})$$

Each one of these spots contributes a finite instability. This means now it would require a finite strength of $V = V_c > 0$ for the condensation to happen. A logarithmic divergence shows up as we approach the perfect nesting limit $\theta \rightarrow 0$. And the $p_x \pm ip_y$ wave exciton gets favored as long as these intersections fall into the $|F_{\mathbf{k}}^{\pm 1}| > |F_{\mathbf{k}}^0|$ region.

For parameters closer to the experimental setup (see caption of Fig.8), we show in Fig.5 the Fermi pockets and band structure before exciton condensation happens. For the model used in the main text (parameter listed in the caption of Fig.2), there is an exact nesting of particle and hole pockets after gauging. In Fig.7(b) we overlay the Fermi surface of this model on top of the color map of the function $\Gamma_{\mathbf{k}} = |F_{\mathbf{k}}^0|^2 - |F_{\mathbf{k}}^1|^2$. This allows us to read off a critical density $n_{A(c)} \sim 0.25$ that is consistent with the transition between s and $p + ip$ exciton order indicated by a red contour in Fig.7(a).

Appendix E: Phase diagram for other values of Φ_A, Φ_B

Fig.8 we show the phase diagram obtained using parameters closer to the experimental system of AB-stacked WSe₂-MoTe₂ bilayer. The phase diagram Fig.8 is qualitatively similar to Fig.2 in the main text. A $p + ip$ instability shows up for exciton density $n_A > 0.35$.

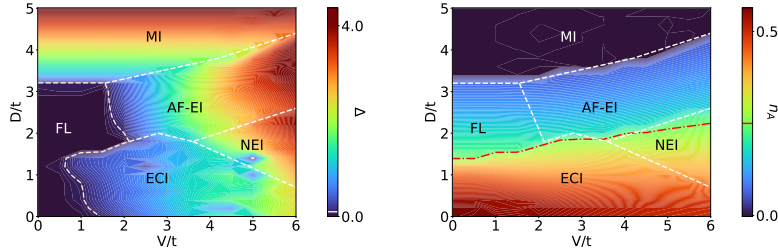


FIG. 8: Schwinger boson mean field phase diagram in $D - V$ plane. (a) Colors show the single electron charge gap Δ_c . We use the following parameters: $U = 50$, $t_A = 2$, $t_B = 1$, $\phi_A = (-2/3 + 1/12)\pi$, $\phi_B = (2/3 + 1/12)\pi$, $V' = 0.5V$. (b) shows the exciton density n_A . The dashed contour in red marks the $n_A = 0.35$, which maps out the phase boundary between ECI and EI.

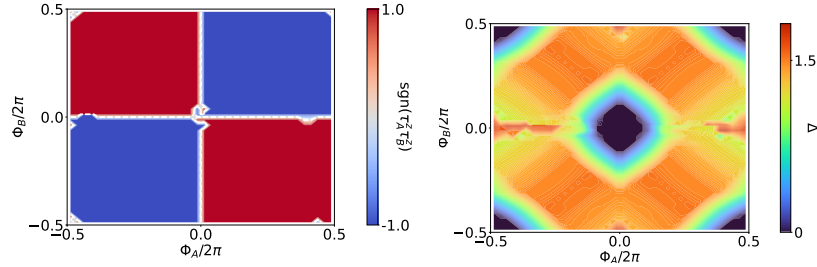


FIG. 9: Hartree-Fock phase diagram for $V = 4.0$, $D = 0.5$. Other parameters are the same as in Fig.2. (a) Sign of $\langle \tau_A^z \tau_B^z \rangle$. (b) Charge gap. For time-reversal breaking phases, there is a two-fold ground state degeneracy. Our convention is to focus on the one with $\langle \tau_A^z \rangle \sim \langle S_A^z \rangle > 0$.

In Fig.9 we show AB valley alignment and charge gap for the same parameter space as in Fig.2. For $\Phi = n\pi$, the model has an enlarged $SU(2) \times SU(2)$ symmetry. Therefore the valley-polarized and spin-polarized states are degenerate. A finite valley contrasting flux breaks the symmetry down to a time reversal, lifting this degeneracy and stabilizing one of the two phases on either side of $\Phi = 0$. For this particular choice of $V/t = 4$, we find Fermi liquid in the vicinity of $\Phi_A = \Phi_B = \pi$ and exciton Chern insulators in a wide range of Φ . As we will find in Fig.11 of Appendix.G, with a stronger V we get a nematic EI at $\Phi \sim 0 \pmod{\pi}$.

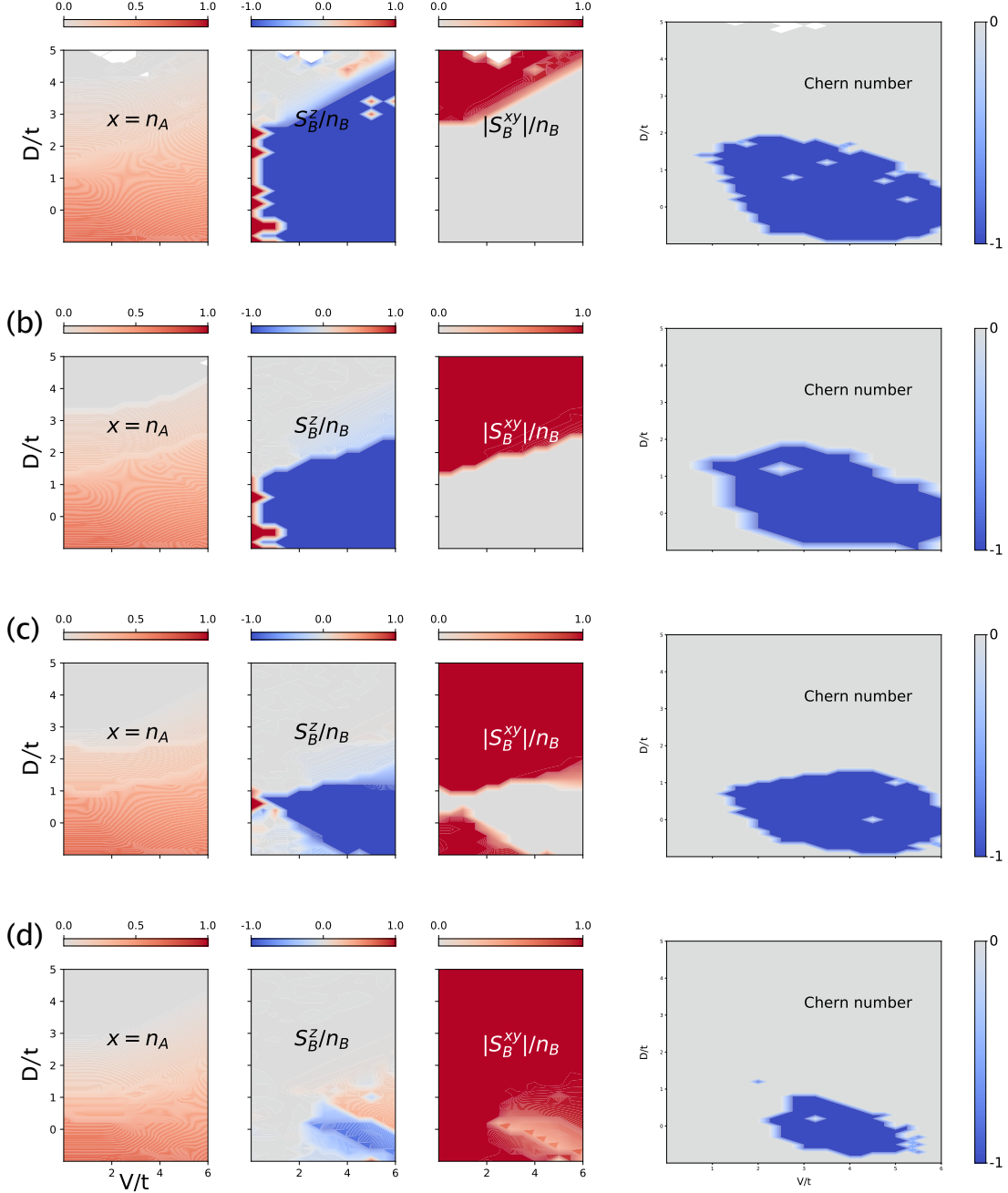


FIG. 10: Schwinger boson mean field phase diagram for $t_A = t_B = 1$, $\phi_A = \pi/4$, $\phi_B = \pi/12$, $V'/V = 0.5$. (a)(b)(c)(d)(e) for $J = 0.001, 0.02, 0.08$ and 0.2 , respectively.

Appendix F: kinetic magnetism and canted spin order

In Fig.10 we show the evolution of the $D - V$ phase diagram calculated for the t-J model in Eq.B3. Focusing on the evolution spin order on the B sublattice as J increases, we find the region with finite in-plane magnetic order expands. At $J = 0.2$, which corresponds to $U/t \sim 20$, the spin order for QAH phase stops being fully polarized to z direction and acquires a 120° AFM component in s_{xy} plane. Namely, in the B layer, we find a 120° in-plane AFM order with canting along the z axis.

Obviously, there is a competition between the super-exchange J term favoring the 120° in-plane magnetic order and kinetic term t_{BB} that stabilizes intra-layer valley polarization. This is reminiscent of Nagaoka ferromagnetism

predicted for the doped square lattice Hubbard model at an extremely strong interaction limit, where kinetic energy dominates over super-exchange and leads to ferromagnetism. Interestingly, for the SU(2) symmetric t-J model on a triangular lattice, due to kinetic frustration, the kinetic energy also favors 120° in-plane magnetic order, hence the t and J term collaborates and there is no magnetic transition as t/J varies. In our case, however, the scenario is complicated by the absence of SU(2) symmetry and by having two sublattices. Eventually, we still observe kinetic ferromagnetism.

This canted spin order is consistent with recent experimental observation⁴⁰. Here we are simply demonstrating the possibility for the exciton condensate to allow a canted order while retaining quantize Hall conductance. In the meantime, we believe the evidence provided by Ref.⁴⁰ alone is not strong enough to rule out other explanations such as phase separation caused by the disorder.

Appendix G: $U(2) \times U(2)$ symmetric point with $\Phi_A = \Phi_B = 0$

At $\Phi_A = \Phi_B = 0$, there is a valley SU(2) symmetry in each layer. In Fig.11 we present the $D-V$ phase diagram for this case. We show in Fig.11(b) the magnitude of order parameters. The $p+ip$ order now appears only in a narrow region around $V = 4.0$, $D = 0$.

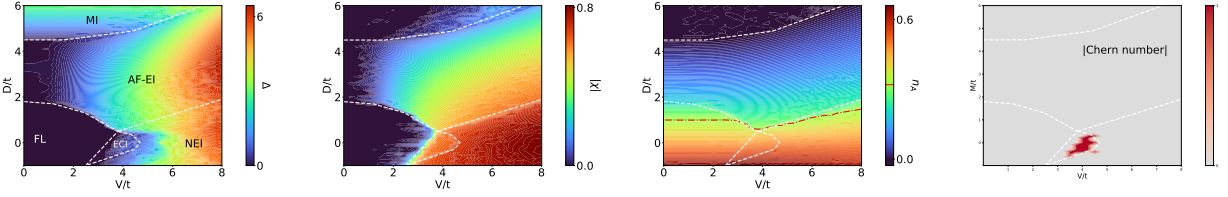


FIG. 11: Schwinger boson mean field phase diagram in $D-V$ plane without valley contrasting flux. $t_{AB} = 0$ and $t_A = t_B = 1$. (a) Charge gap. (b) The magnitude of exciton order. (c) Exciton density. (d) Chern number.

We start our discussion from the low exciton density regime $n_A \sim 0$. As before, we find the AF-EI phase with s wave exciton order at small exciton density. But now the AF-EI phase is more robust and the NEI phase with p wave exciton order starts only when $n_A > 0.35$. The reason is the following. With the τ_z polarized in both layers, there are two degenerate holon pockets from B layer around \mathbf{K}_M and \mathbf{K}'_M points, and one electron pocket from A layer at $\mathbf{\Gamma}_M$. In this case exciton order only hybridizes one of the hole pockets with the electron pocket and is not effective to gap out the electron-hole pocket. This penalizes the energy of the FM phase. On the other hand, with the 120° AF order in the B layer, there is only one hole pocket at $\mathbf{\Gamma}_M$ and an s wave exciton order effectively gaps out the electron pocket and the hole pocket. So the AF EI phase has better energy and occupies larger phase regions when $\Phi_A = \Phi_B = 0$.

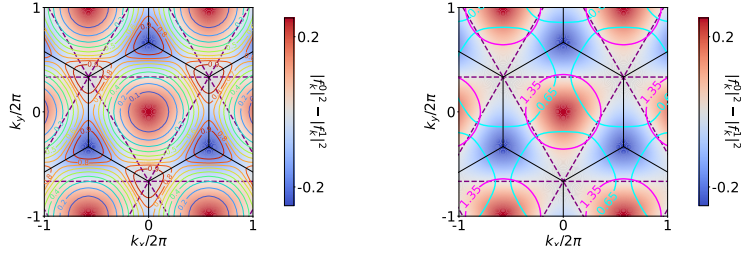


FIG. 12: (a) Form factor difference between $l = 1$ and $l = 0$ channels. The overlaid contours are Fermi surfaces at various fillings for a triangular lattice tight-binding model with no hopping phases. This plot helps determine pairing instability when the B layer is in 120° magnetic order so that the holon and particle bands are perfectly nested. Numbers labeling these contours correspond to the n_A associated with the two Fermi surfaces. (b) Gauged Fermi surfaces for $n_A = 0.35$. The gauge choice is such that the two pockets are both centered at $\mathbf{\Gamma}_M$. At this density, the intersections between two Fermi surfaces enter the region where $p+ip$ pairing is stronger than that of s wave.

On the other hand, consider the competing state with ferromagnetic order in B layer. In contrast to the AFM state, with an FM background, there is no π Berry flux contributed by the spin configuration. As a result, the holon

band gets inverted, and the Fermi surface now sits in the vicinity of \mathbf{K}_M and \mathbf{K}'_M , where the p wave form factors $F_{\mathbf{k}}^{\pm 1}$ dominate over that of s wave (see orange contour in Fig.12(a), or blue contour in Fig.12(b) for the holon pocket after gauging). So we get the ECI phase with τ_z FM when $n_A > 0.35$. However, the ECI phase is quite fragile and unstable to the nematic EI (NEI) phase for this parameter. To get a robust Chern insulator, a small valley contrasting flux Φ_A or Φ_B is needed.

Appendix H: Competition between band Chern insulator and excitonic insulator with t_{AB}

With a strong enough t_{AB} to hybridize the two layers, a band Chern insulator (bCI) with canted 120° antiferromagnetic order was found in a previous study⁴⁵. Note here band Chern insulator may not be a good name because the phase apparently still requires strong intra-layer repulsion to generate the AF order. Here we mainly focus on the effective Hamiltonian H_f of the charge part after the magnetic order is fixed. Then the phase in Ref. 45 is realized in the large t_{AB} but small V limit. The hopping of f is decided entirely by the original single electron hopping t_{AB} and we call it band insulator to distinguish it from the excitonic insulator in this paper. In Fig.13 we investigate the transition from this band Chern insulator to our interaction-driven exciton insulators by turning on the repulsion V and V' . In presence of a t_{AB} term, the U(1) symmetry associated with layer charge conservation is explicitly broken.

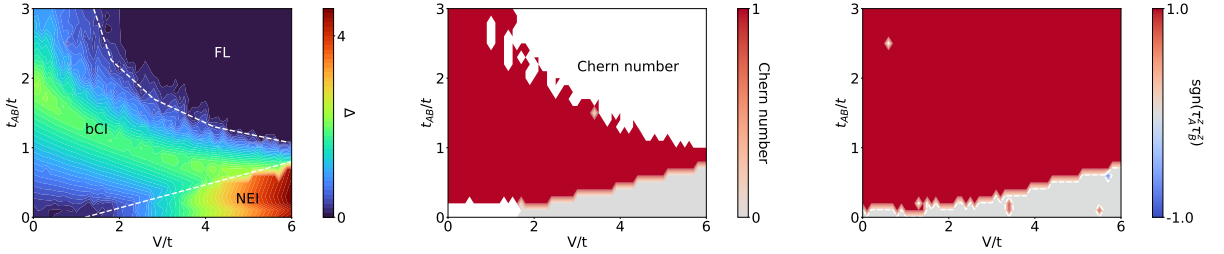


FIG. 13: Hartree-Fock phase diagram in $t_{AB} - V$ plane. (a) Charge gap. (b) Chern number. (c) The sign of $\tau_A^z \tau_B^z$ when it is nonzero. This phase diagram is calculated using the same set of parameters as in Ref45, $t_A = t_B = 1$, $\Phi_A = 2\pi$, $\Phi_B = 0$, and $D = 3$.

The effective hopping of the bCI phase is actually equivalent to the $p + ip$ exciton order in our ECI phase. To simplify the discussion, we follow the Schwinger boson mean field theory, where spin magnetic order contributes to the charge part through the Berry phase. The mean field Hamiltonian for the charge part is again purely a spinless model:

$$\begin{aligned}
 H_c^{MF} = & - \sum_{\langle i,j \rangle_{A,B}} t_{AB} (F_i^{a\dagger} F_j^a) f_i^\dagger f_j + h.c. \\
 & - \sum_{a=A,B} \sum_{\langle\langle ij \rangle\rangle_a} t_a (F_i^{a\dagger} e^{i\phi_{ij;a}\tau_z} F_j^a) f_i^\dagger f_j + h.c. \\
 & - V \sum_{\langle ij \rangle} \chi_{ji} f_i^\dagger f_j + D \sum_{i \in A} n_i - D \sum_{j \in B} n_j
 \end{aligned} \tag{H1}$$

And we will define the effective charge-hopping phase as

$$t_{ij;a}^f = t_a (F_i^{a\dagger} e^{i\phi_{ij;a}\tau_z} F_j^a) = \tilde{t}_a e^{i\tilde{\phi}_a} \tag{H2}$$

along with effective flux $\tilde{\Phi}_a = 3\tilde{\phi}_a$. $\chi_{ji} = \langle f_i^\dagger f_j \rangle$ gives the exciton order. The bCI has a full τ_z polarization in layer A. In layer B it has a 120° order in τ_{xy} plane, along with a uniform τ^z component, which satisfies $\langle \tau_A^z \tau_B^z \rangle > 0$. The Schwinger boson mean field ansatz is

$$F_i^A = (1, 0)^T \tag{H3}$$

$$F_j^B = e^{\frac{i}{2}(\sigma^z + \mathbb{1})\mathbf{K} \cdot \mathbf{r}_j} \left(\cos \frac{\theta}{2}, \sin \frac{\theta}{2} \right)^T \tag{H4}$$

where $\theta \in (0, \pi/2)$ is the angle of canting.

There is a competition between t_{AB} and V . At $V = 0$ and before layer hybridization, both the electron pocket of the A layer and the holon pocket of the B layer is centered at \mathbf{K}_M under the gauge choice of Eq.H3. The effect of t_{AB} term is similar to that of mean field Hamiltonian $H_V = -V \sum_{\langle ij \rangle} \chi_{ji} f_i^\dagger f_j$ when $\chi_{Q,L} \neq 0$ for $Q = L = 0$, namely, a completely uniform distribution of exciton order on every bond. To match the discussion of Sec. C, we gauge the electron and hole pockets back to $\mathbf{\Gamma}_M$ by a gauge transformation

$$\begin{aligned} f_{A,i} &\rightarrow f_{A,i} e^{-i\mathbf{K}\cdot\mathbf{r}_i} \\ f_{B,j} &\rightarrow f_{B,j} e^{-i\mathbf{K}\cdot\mathbf{r}_j} \end{aligned} \quad (\text{H5})$$

under which the t_{AB} term becomes

$$t_{AB} f_{A,i}^\dagger f_{B,j} \rightarrow t_{AB} e^{i\mathbf{K}\cdot(\mathbf{r}_j - \mathbf{r}_i)} f_{A,i}^\dagger f_{B,j} = \tilde{t}_{AB} f_{A,i}^\dagger f_{B,j} \quad (\text{H6})$$

Now the new inter-layer tunneling \tilde{t}_{AB} transforms non-trivially under C_3 rotations. At the mean-field level for f , this \tilde{t}_{AB} is equivalent to the $p + ip$ exciton order in the ECI phase. So the charge part of the bCI and our ECI has the same mean-field ansatz; thus, both have $C = 1$. When increasing the V term, exciton order χ_{ij} decoupled from the interaction dominates over the t_{AB} term. At low density, s wave exciton condensation is favored. Hence the effective hopping now has both the $p + ip$ component from the external t_{AB} term and s component from exciton order. Consequently, we expect an NEI with $s + p$ exciton order. This NEI has 120° magnetic order in both layers with the same chirality and no τ_z polarization. This is demonstrated in Fig.13(c). The strongest bond connects the two AB sites with parallel valley τ_{xy} . So this NEI is connected to the s wave AF-EI phase we found earlier at $t_{AB} = 0$. For the parameter $\Phi_A = 2\pi, \Phi_B = 0$ here, the ECI phase is quite fragile as shown in the previous section. But if we choose a different flux Φ , the bCI phase can be driven into the ECI phase by increasing V . Note although both the bCI and the ECI have the same $p + ip$ order in the mean-field level of the electron and holon f , their magnetic orders are different and there must still be a phase transition between them.

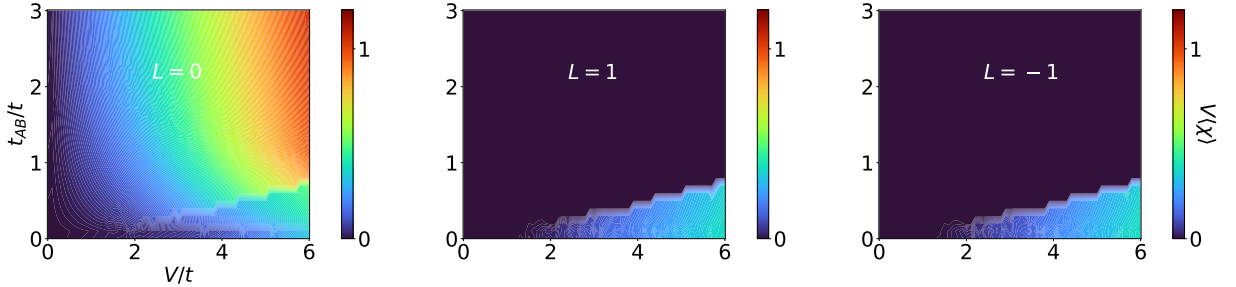


FIG. 14: Order parameter in each angular momentum channel. This is the result before gauging. After the gauge transform (see text), the angular momentum quantum number L gets shifted by 1.

The bCI phase by Ref. 45 and our ECI phase have the same origin of the non-zero Chern number. But there are some essential differences: (1) The effective hopping in the ECI phase is spontaneously generated from inter-layer Coulomb interaction while the hopping of the bCI phase inherits from single electron hopping t_{AB} . (2) The $p \pm ip$ exciton order of the ECI phase does not rely on the 120° magnetic order in the B layer. Actually, in our ECI phase, both layers are fully valley polarized. On the other hand, 120° order is essential for the bCI phase. (3) The bCI picture is appropriate only when the inter-layer interaction V is small. In the real system the inter-layer tunneling t_{AB} is small, but the repulsion V is quite large. So we should be in the limit $t_{AB} \ll t_A \ll V$. Thus the effective hopping of the charge f is dominated by the exciton order $V\chi_{ij}$, which could be s wave or $p \pm ip$ depending on parameters. In the small t_{AB} , large V regime appropriate to realistic systems, the bCI is unstable, and a Chern insulator phase, if exists, should originate from exciton order as in our ECI phase.

Appendix I: Excitonic topological insulator at $\nu_T = 2$

Let us also have some discussions for the total filling $\nu_T = n_A + n_B = 2$. When D is large, the ground state should be a band insulator with two electrons per triangular site on the B layer while the A layer is empty. Again electrons are transferred to the A layer when D is decreased. Experimentally a topological insulator with helical edge modes is observed at $\nu_T = 2^{27}$ for intermediate values of D . Presumably, two Chern bands with $C = \pm 1$ are occupied. Each Chern band can be described by a mean-field theory similar to our discussion at $\nu_T = 1$ and can still arise

from the excitonic mechanism. Both intra-valley and inter-valley exciton condensation are possible, leading to either a quantum valley Hall (QVH) insulator or a quantum spin Hall (QSH) insulator. QVH insulator can crossover to a band insulator from pure single particle physics. QSH insulator has additional inter-valley-coherent (IVC) order and maybe a parent state of superconductivity upon doping^{32,55,56}. We hope future experiments can distinguish these two different states.